

Atomic design of dual-metal hetero-single-atoms for high-efficiency synthesis of natural flavones

Received: 19 August 2022

Accepted: 12 December 2022

Published online: 22 December 2022

 Check for updatesXin Zhao¹, Ruiqi Fang¹  , Fengliang Wang¹, Xiangpeng Kong² & Yingwei Li^{1,3}  

Single-atom (SA) catalysts provide extensive possibilities in pursuing fantastic catalytic performances, while their preparation still suffers from metal aggregation and pore collapsing during pyrolysis. Here we report a versatile medium-induced infiltration deposition strategy for the fabrication of SAs and hetero-SAs ($M_aN_4/M_bN_4@NC$; $M_a = Cu, Co, Ni, Mn$, $M_b = Co, Cu, Fe$, $NC = N$ -doped carbon). In-situ and control experiments reveal that the catalyst fabrication relies on the “step-by-step” evolution of M_a -containing metal-organic framework (MOF) template and M_b -based metal precursor, during which molten salt acts as both pore generator in the MOF transformation, and carrier for the oriented infiltration and deposition of the latter to eventually yield metal SAs embedded on hierarchically porous support. The as-prepared hetero-SAs show excellent catalytic performances in the general synthesis of 33 kinds of natural flavones. The highly efficient synthesis is further strengthened by the reliable durability of the catalyst loaded in a flow reactor. Systematic characterizations and mechanism studies suggest that the superior catalytic performances of $CuN_4/CoN_4@NC$ are attributed to the facilitated O_2 activating-splitting process and significantly reduced reaction energy barriers over CoN_4 due to the synergetic interactions of the adjacent CuN_4 .

Metal catalysts are widely used in modern chemical industry. Pyrolysis is the most commonly employed protocol to prepare heterogeneous metal-based catalysts with sizes from atom-scale (including single-atom (SA) and subnanocluster) to nanoscale and beyond^{1–5}. Nevertheless, structural and compositional evolutions of the pyrolysis precursors at high temperatures are considerably intricate, leading to high difficulty in the controllable construction of uniform sites especially at atomic level. For the metal species, the high surface free energies usually lead to unwilling aggregations (i.e., Ostwald ripening)^{6–8}. To improve the dispersion, strategies like reducing the content, partial evaporation or changing the topology of metal precursors have been developed, but the formation of metal-metal bonds is still not fundamentally avoided. In terms of the non-metal species (e.g., carbons and

heteroatoms), which are generally transformed into supports or coordinated-atoms after pyrolysis, circumstances are even complex. At high temperatures, the inconsistent physicochemical properties (e.g., chemical environment, thermal stability and spatial distribution) of these non-metal species usually result in uncontrollable decomposition of the precursors^{9–12}. Besides, the carbonization and subsequent atom migration processes are also highly random, and the evaporation and removal of non-metal components could possibly cause pore generation/collapsing and even dimension changes (e.g., from 3D to 2D)^{13,14}. All these factors make the materials synthesis highly unpredictable. So far, it is still highly demanded to develop versatile and controllable pyrolysis synthesis routes to fundamentally understand the preparation of metal-based catalysts.

¹State Key Laboratory of Pulp and Paper Engineering, School of Chemistry and Chemical Engineering, South China University of Technology, Guangzhou 510640, China. ²The School of Materials Science and Engineering, Harbin Institute of Technology, Shenzhen 518055, China. ³South China University of Technology–Zhuhai Institute of Modern Industrial Innovation, Zhuhai 519175, China. ✉e-mail: fangrq@scut.edu.cn; liyw@scut.edu.cn

In this work, we demonstrate an effective and versatile medium-induced infiltration deposition strategy, which can simultaneously realize the monodispersion of metal species and controllable transformation of non-metal species for the synthesis of a series of SAs or hetero-SAs embedded on N-doped carbons ($M_aN_4/M_bN_4@NC$, $M_a = Cu, Co, Ni, Mn$; $M_b = Co, Cu, Fe$). Well-defined M_a -containing metal-organic frameworks (MOFs) and M_b -based phthalocyanine (Ph) are employed as pyrolysis precursor with a mixed molten salt (KCl-KBr) as medium. During pyrolysis, in-situ and control experiments directly reveal the morphology evolution of the template inside the medium. Systematical characterizations of $M_aN_4/M_bN_4@NC$ indicate the homogeneous distribution of both M_aN_4 and M_bN_4 sites throughout the carbons with inter-connecting hierarchical porosity. Specifically, $CuN_4/CoN_4@NC$ shows attractive catalytic performances in the domino synthesis of a wide range of flavones in both batch and flow reactor. A combination of experimental and density functional theory (DFT) results demonstrate that the high reactivity of $CuN_4/CoN_4@NC$ is attributable to the enhanced O_2 activation capability, and reduced reaction energy barriers over CoN_4 arising from the synergetic interactions of CuN_4 . Moreover, the inter-connecting hierarchical pores can largely facilitate the mass transfer and promote the accessibility of hetero-SA sites.

Results

Synthesis and characterization of $CuN_4/CoN_4@NC$

The proposed medium-induced infiltration deposition strategy is of considerable flexibility and generality for the fabrication of various dual-metal hetero-SAs (Supplementary Figs. 1–3, Supplementary

Tables 1–2) and single metallic SAs (Supplementary Figs. 4, 5, 12f, 13f, and Supplementary Tables 3–4). Preliminary analysis implies the Cu and Co SA sites are active in O_2 activation and domino reaction (including condensation, cyclization and oxidative dehydrogenation), respectively. Therefore, the preparation of $CuN_4/CoN_4@NC$ (schematically illustrated in Fig. 1a) is selected as a proof of concept to clarify some key details. Initially, uniform Cu-modified bimetallic zeolitic imidazolate framework (Cu -ZIF-8) crystals were assembled (Supplementary Figs. 6a, 7b)¹⁵. Next, Cu -ZIF-8 was mixed with a medium (i.e., a mixture of KCl and KBr salts) and Co-Ph. The obtained mixture was subjected to pyrolysis under Ar at 750 °C, which is higher than the decomposition temperatures of both Cu -ZIF-8 and Co-Ph (as determined by thermogravimetric analysis, Supplementary Fig. 6b, c). At high temperatures, Zn species are partially removed, and the salt medium melts and carries the Co-Ph to infiltrate into the Cu -ZIF-8 interior, during which the decomposition of Cu -ZIF-8 is accelerated with the formation of CuN_4 and CoN_4 sites embedded on the N-doped carbon support ($CuN_4/CoN_4@NC$). After pyrolysis, the KCl-KBr gradually seeds out, leaving the hierarchical interior of the as-prepared materials with micro- and meso- as well as macro-pores. The catalyst yield is about 42% (Supplementary Table 5).

Scanning electron microscopy (SEM) images (Fig. 1b) of $CuN_4/CoN_4@NC$ show a rhombic dodecahedral morphology with a size of ca. 1 μm , and the high porosity is clearly observed from one broken particle (Fig. 1c). The porous interior and thin walls (ca. 10 nm in thickness) is further verified by the transmission electron microscopy (TEM) photographs (Fig. 1d and Supplementary Fig. 8). The low-dose

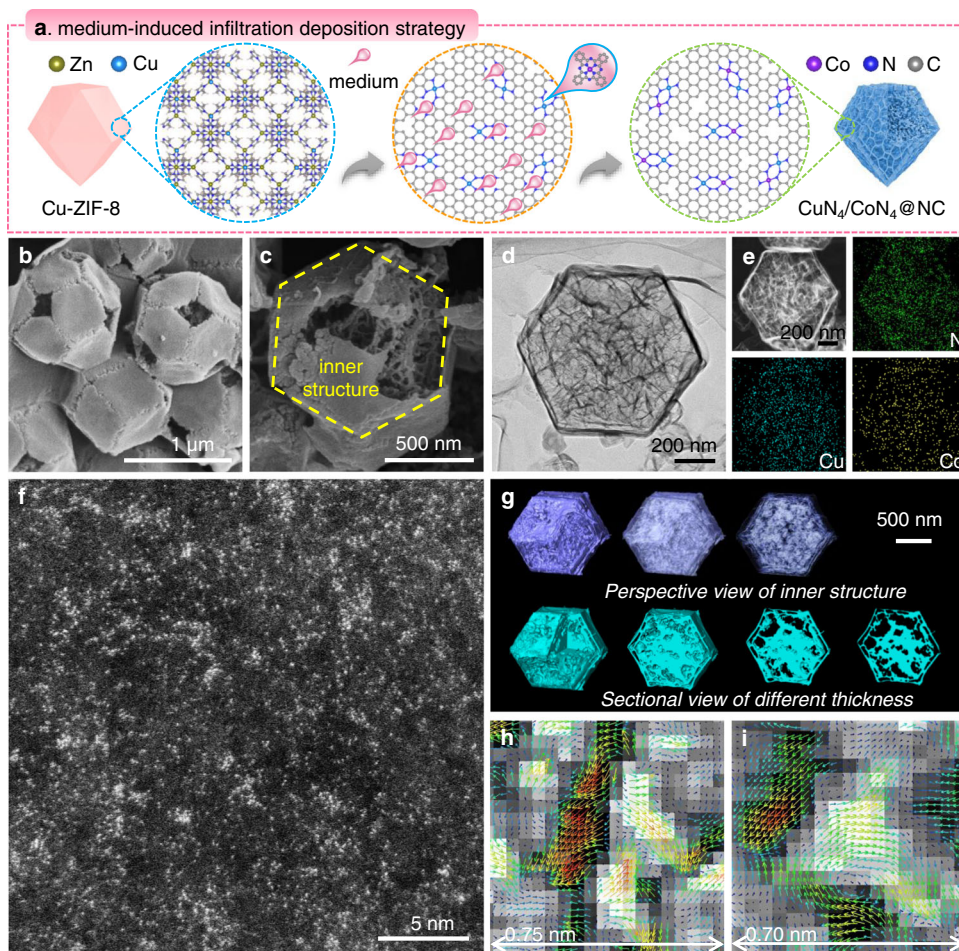


Fig. 1 | Synthesis and structural characterizations of $CuN_4/CoN_4@NC$. a Schematic illustration of the synthesis strategy. b, c SEM, d TEM, e HAADF-STEM and corresponding elemental mapping, and f AC HAADF-STEM image. g 3D

reconstruction of a $CuN_4/CoN_4@NC$ particle by HRTEM electron tomography. h, i DPC-STEM images.

high-resolution TEM (HRTEM) tomography is additionally conducted upon an individual particle to thoroughly study the topological morphology of $\text{CuN}_4/\text{CoN}_4@\text{NC}$ (Fig. 1g, Supplementary Movies 1 and 2). In the perspective view, the shell of dodecahedron is tuned partially transparent to show the topology. As expected, the porous interior with inter-connecting pores is clearly observed. Besides, in the sectional views, TEM photographs of the particle with different thickness also demonstrate the homogeneous distribution of hierarchical pores. N_2 isotherms and pore size distributions (Supplementary Fig. 9a, b, and Supplementary Table 2) further verify the hierarchical pore structure inside $\text{CuN}_4/\text{CoN}_4@\text{NC}$ with a high Brunauer-Emmett-Teller (BET) specific surface area of $1112.2 \text{ m}^2 \text{ g}^{-1}$.

High-angle annular dark-field scanning transmission electron microscopy (HAADF-STEM) and corresponding elemental mappings (Fig. 1e) indicate the homogeneous distribution of Cu and Co species. The content of Cu and Co in $\text{CuN}_4/\text{CoN}_4@\text{NC}$ is 1.46 and 1.42 wt% (Supplementary Table 2), respectively. Spherical aberration-corrected HAADF-STEM (AC HAADF-STEM) image (Fig. 1f) demonstrates the isolated metal single-atoms including Cu and Co (bright dots), as different metals could not be clearly identified through limited Z-contrast differences. Supplementary Fig. 10 The homogeneous distribution of uniform Cu and Co atomic sites contributes to the formation of non-spherical Coulomb field in their adjacent regions (displayed by arrows in Fig. 1h, i, and Supplementary Fig. 11)¹⁶. The resultant electron transfer tendency in selected areas is clearly revealed via differential phase contrast (DPC) STEM. Under the influence of as-formed Coulomb field, carbonous support tends to donate electrons towards the immobilized metal SA sites.

Powder X-ray diffraction (XRD) patterns (Supplementary Fig. 9c) of $\text{CuN}_4/\text{CoN}_4@\text{NC}$ display a broad peak centered at 26.2° , suggesting the MOF ligands have been transformed into graphitic carbon species¹⁷. The presence of defects is verified by Raman analysis (Supplementary Fig. 9d), showing an I_D/I_G value of ca. 1.12. Notably, no obvious characteristic diffraction of Cu or Co species is detected (Supplementary Fig. 9c), possibly due to their atomic dispersions. In $\text{CuN}_4/\text{CoN}_4@\text{NC}$, the N content is relatively high (13.4 wt%, Supplementary Table 2) with the dominance of pyridinic-N and graphitic-N species (Supplementary Fig. 9e). The C 1s X-ray photoelectron spectroscopy (XPS, Supplementary Fig. 9f) suggests the significant fraction of C-N species arising from the high N content¹⁸. Moreover, the Zn 2p XPS analysis (Supplementary Fig. 12) indicates negligible Zn residues in the as-synthesized $\text{CuN}_4/\text{CoN}_4@\text{NC}$.

Atomic structure analysis of $\text{CuN}_4/\text{CoN}_4@\text{NC}$

X-ray absorption fine structure (XAFS) spectra were recorded to elucidate the electronic structures of Cu and Co species in $\text{CuN}_4/\text{CoN}_4@\text{NC}$ at atomic level (Fig. 2, Supplementary Figs. 13, 14, and Supplementary Table 6). A few Cu- or Co-based standard samples (e.g., Cu foil, Cu_2O , CuO, Co foil, CoO, and Co_3O_4) and composites (Cu-ZIF-8 and Co-Ph) were utilized as references. Cu K-edge X-ray absorption near-edge structure (XANES) spectrum (Fig. 2a) of $\text{CuN}_4/\text{CoN}_4@\text{NC}$ situates between that of Cu^0 and Cu^{2+} , suggesting a valence state of 0 to +2 for the Cu species. The high similarity of $\text{CuN}_4/\text{CoN}_4@\text{NC}$ and Cu-ZIF-8 spectra implies similar coordination configurations of their Cu moieties. The Fourier-transformed (FT) k^3 -weighted extended X-ray absorption fine structure (EXAFS) spectrum (Fig. 2b) of Cu in $\text{CuN}_4/\text{CoN}_4@\text{NC}$ exhibits a significant peak at 1.5 \AA (like Cu-ZIF-8), which can be attributed to the Cu-N coordination. Notably, no Cu-Cu coordination peaks at around 2.24 \AA are detected, confirming the single-atom distribution (rather than aggregation) of Cu in $\text{CuN}_4/\text{CoN}_4@\text{NC}$. The EXAFS fitting curves (Fig. 2c) recover a N_4 coordination configuration of Cu with a Cu-N bond length of 1.96 \AA (Supplementary Table 6). The maximum at 4.0 \AA^{-1} in wavelet transform (WT)-EXAFS of $\text{CuN}_4/\text{CoN}_4@\text{NC}$ (Fig. 2h) is assigned to Cu-N bonding, in good accordance with Cu-ZIF-8.

Similarly, the Co K-edge XANES spectra (Fig. 2i) of $\text{CuN}_4/\text{CoN}_4@\text{NC}$ display a near-edge absorption between Co foil and CoO, suggesting a valence state of lower than +2. The similar peak location of $\text{CuN}_4/\text{CoN}_4@\text{NC}$ and Co-Ph indicates analogous coordination configurations of their Co species. The increased peak intensity of $\text{CuN}_4/\text{CoN}_4@\text{NC}$ is ascribed to the distorted D_{4h} symmetry possibly resulting from the Cu-N₄ sites^{19,20}. The FT k^3 -weighted Co EXAFS spectrum (Fig. 2j) of $\text{CuN}_4/\text{CoN}_4@\text{NC}$ shows one remarkable peak at 1.43 \AA , very close to that of Co-Ph (1.44 \AA). As no Co-Co coordination peaks (2.16 \AA) are detected, we could infer the Co single-atoms are predominantly coordinating to N. Moreover, the Co K-edge EXAFS fitting curves (Fig. 2k) match well with the proposed structural models. The optimized fitting parameters (Supplementary Table 6) suggest each Co atom is coordinating to four N atoms with a bond length of ca. 1.98 \AA , as is also verified by the highly similar WT-EXAFS spectra of $\text{CuN}_4/\text{CoN}_4@\text{NC}$ and Co-Ph.

Possible formation mechanism of $\text{CuN}_4/\text{CoN}_4@\text{NC}$

To interpret the structural evolution process and formation mechanism of $\text{CuN}_4/\text{CoN}_4@\text{NC}$, some control experiments were carried out (Supplementary Table 1). To disclose the role of salt medium, $\text{CoN}_4@\text{NC}$ and $\text{CuN}_4@\text{NC}$ were prepared via the similar procedures (Supplementary Figs. 4, 5, 13f, 14f, and Supplementary Tables 2–4). Specifically, pristine ZIF-8 was employed as precursor for the preparation of $\text{CoN}_4@\text{NC}$. The obtained material features inter-connecting porosity and thin shells, throughout which atomic Co sites are clearly observed. The Co K-edge XANES and EXAFS spectra of $\text{CoN}_4@\text{NC}$ demonstrate the atomic affixing of Co on N-doped carbon via Co-N₄ coordination. $\text{CoN}_4@\text{NC}$ possesses a relatively higher BET specific surface area ($1598.7 \text{ m}^2 \text{ g}^{-1}$) with more micro- and mesopores than $\text{CuN}_4/\text{CoN}_4@\text{NC}$. The successful preparation of $\text{CoN}_4@\text{NC}$ implies the carrier role of salt medium in the infiltration of Co-Ph through the pores/channels of ZIF-8. To further elucidate this, $\text{CuN}_4@\text{NC}$ was also fabricated in the absence of Co-Ph (Supplementary Fig. 4 and Supplementary Tables 2–5). The enhanced specific surface area ($2070.1 \text{ m}^2 \text{ g}^{-1}$) is possibly ascribing to the absence of Co-Ph (and derivatives) which might block the pores.

However, in the absence of salt medium, significant metallic aggregations are observed over the as-obtained $\text{Cu}_x/\text{Co}_x@\text{NC}$ -750 (Supplementary Fig. 15 and Supplementary Table 2). The aggregated Co species around rhombic dodecahedra are derived from Co-Ph, which could not migrate into the interior of Cu-ZIF-8 without a salt medium. The small specific surface area ($144.0 \text{ m}^2 \text{ g}^{-1}$) and reduced micropore fraction is possibly related to the sluggish generation and coalescence process of pores. These results demonstrate the essential roles of salt medium in Co-Ph diffusion and hierarchical pore generation. The successful preparation of $\text{CoN}_4@\text{NC}$ and $\text{CuN}_4@\text{NC}$ suggests the high potential of the present strategy in fabricating single metallic SAs through simply modifying the MOF or metal precursor.

On the basis of the above results, a plausible mechanism is proposed for the synthesis of $\text{CuN}_4/\text{CoN}_4@\text{NC}$ via the developed medium-induced infiltration deposition strategy. At the beginning of the heating process, KCl-KBr plays the role of carrier, which melts and carries the Co-Ph precursor to infiltrate into the pores/channels of Cu-ZIF-8 by capillarity (as disclosed by in-situ TEM experiment, Supplementary Fig. 16 and Supplementary Movie 3). When the temperature reaches 600°C , the decomposition of Cu-ZIF-8 begins (Supplementary Fig. 6b), during which the KCl-KBr medium acts as both carbonization booster and metal stabilizer. As a result, the graphitization of organic ligands is remarkably accelerated (Supplementary Figs. 9d and 15n), and the agglomeration of metal nodes is suppressed due to the formation of M-X complexes ($M = \text{Zn}, \text{Cu}$ and Co ; $X = \text{Cl}$ and Br). Notably, the presence of KCl-KBr leads to a time difference between the decomposition of Cu-ZIF-8 and Co-Ph, which is crucial to avoid the formation of metal-metal bonds during the “step-by-step” evolution from Cu-ZIF-8 and Co-Ph to $\text{CuN}_4/\text{CoN}_4@\text{NC}$. On the other hand, the

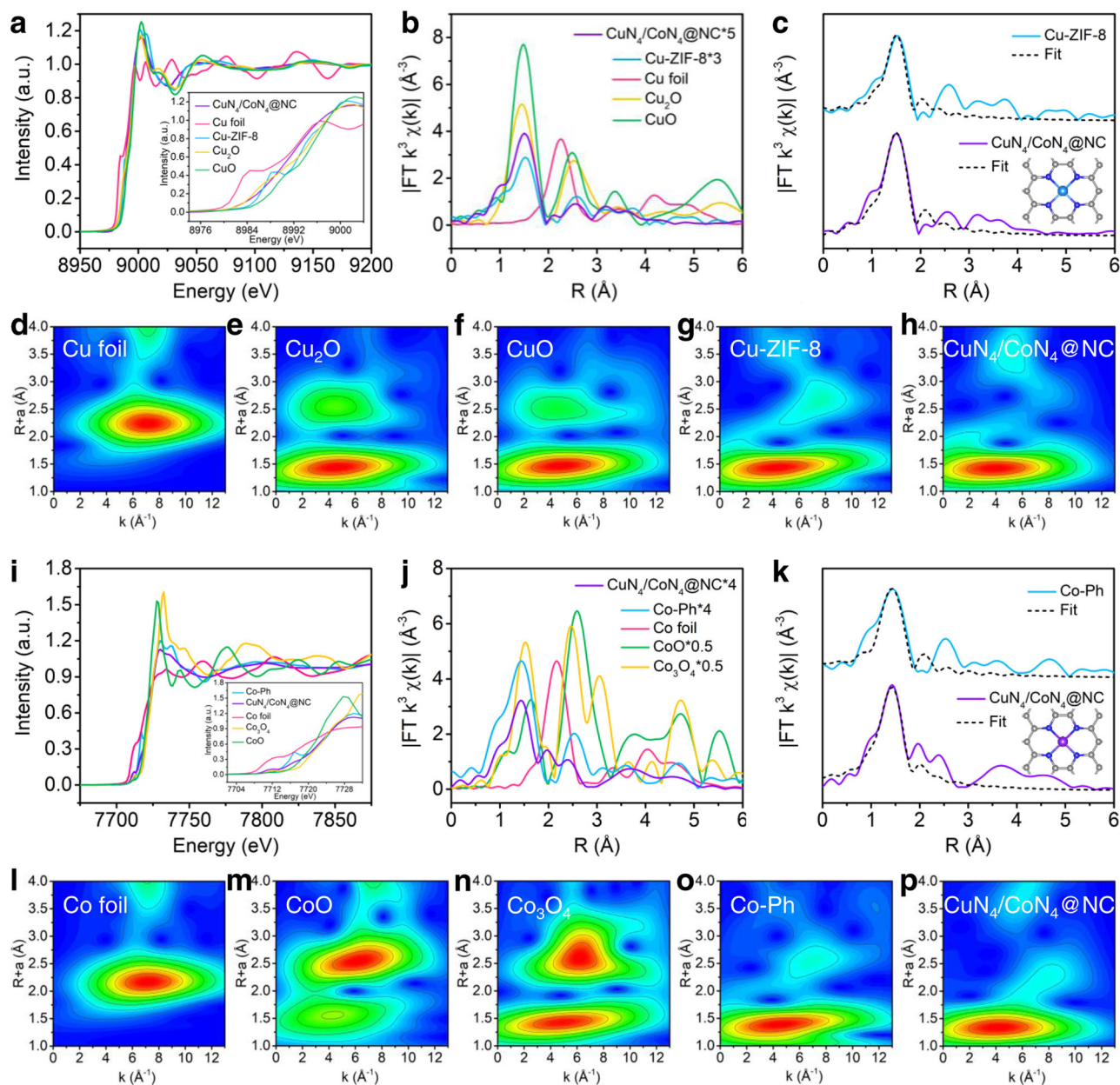


Fig. 2 | Atomic structural analysis of $\text{CuN}_4/\text{CoN}_4@\text{NC}$. **a** Cu K-edge XANES spectra, **b** Fourier-transformed (FT) k^3 -weighted EXAFS spectra for the Cu K-edge, **c** Cu K-edge EXAFS fitting curves of $\text{CuN}_4/\text{CoN}_4@\text{NC}$ and Cu-ZIF-8 in R space (inset: model of CuN_4 sites), **d–h** Wavelet-transformed k^3 -weighted EXAFS spectra. **i** Co

K-edge XANES spectra, **j** FT k^3 -weighted EXAFS spectra for the Co K-edge, **k** Co K-edge EXAFS fitting curves of $\text{CuN}_4/\text{CoN}_4@\text{NC}$ and Co-Ph in R space (inset: model of CoN_4 sites), **l–p** Wavelet-transformed k^3 -weighted EXAFS spectra.

molten salt could also facilitate the generation of defects, which gradually migrate and coalesce into micro-, meso- and even macropores at high temperature. In the cooling process, KCl-KBr gradually seeds out and helps retaining the as-formed inter-connecting channels within the carbon support (Supplementary Movies 1 and 2). Eventually, the CuN_4 and CoN_4 sites are affixed on the N-doped carbons with hierarchical porosity.

DFT calculations (Fig. 3, Supplementary Fig. 17, and Supplementary Table 7) are additionally performed to verify the key issues of the proposed formation mechanism of $\text{CuN}_4/\text{CoN}_4@\text{NC}$. The structural model of pristine Cu-ZIF-8 is simplified as $\text{CuN}_4/\text{ZnN}_4@\text{NC}$, and the KCl-KBr medium in molten state is established as $\text{K}_8\text{Cl}_2\text{Br}_6$ (or $\text{K}_{16}\text{Cl}_4\text{Br}_{12}$). In $\text{CuN}_4/\text{ZnN}_4@\text{NC}$, the positively charged Cu and Zn atoms tend to coordinate with Cl^- and Br^- anions. The adsorption energy of Cu atom to Cl^- and Br^- is -0.63 eV (Supplementary Fig. 17),

higher than that of Zn atom (-1.25 or -1.20 eV, respectively). In this concern, it is relatively easier for Zn, in comparison with Cu, to bond with Cl^- and Br^- . Due to the lower energy, Zn is more inclined to combine with Cl^- to form $\text{CuN}_4/\text{ZnN}_4@\text{NC-K}_{16}\text{Cl}_4\text{Br}_{12}$ (Fig. 3, step A), as indicated by red circle and arrow. Subsequently, Zn species are removed from $\text{CuN}_4/\text{ZnN}_4@\text{NC}$ by molten salt in the form of $\text{Zn-K}_8\text{Cl}_2\text{Br}_6$ (Fig. 3, step B), and the energy change of this process is -0.54 eV. Next, the $\text{Co-K}_8\text{Cl}_2\text{Br}_6$ (generated in a similar way to $\text{Zn-K}_8\text{Cl}_2\text{Br}_6$) locates onto the as-formed vacancy (vac) in the residue $\text{CuN}_4/\text{vacN}_4@\text{NC-K}_{16}\text{Cl}_4\text{Br}_{12}$ with Co atom coordinating to four N atoms to form $\text{CuN}_4/\text{CoN}_4@\text{NC-K}_{16}\text{Cl}_4\text{Br}_{12}$ (Fig. 3, step C), and the energy change of this process is -1.59 eV. Finally, $\text{CuN}_4/\text{CoN}_4@\text{NC}$ is obtained after the removal of $\text{K}_8\text{Cl}_2\text{Br}_6$ by thorough washing.

Some control experiments were then conducted to uncover the key details in the formation of $\text{CuN}_4/\text{CoN}_4@\text{NC}$. The molten salt

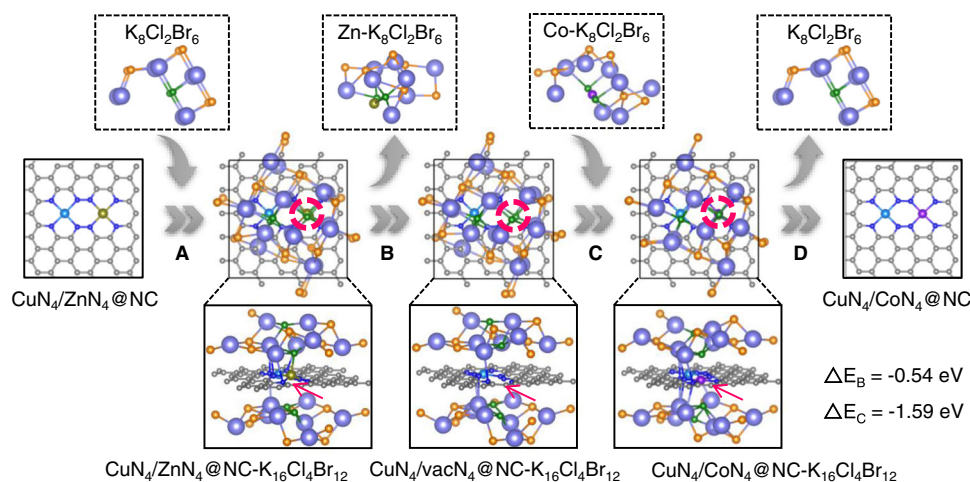


Fig. 3 | Mechanism of the synthesis strategy. Proposed mechanism for the formation of $\text{CuN}_4/\text{CoN}_4@\text{NC}$.

could facilitate the removal of Zn (rather than Cu) through coordination. To elucidate this, eight possible circumstances (including single/double metallic counterparts with and without $\text{K}_8\text{Cl}_2\text{Br}_6$ in the system, Supplementary Fig. 18) are simulated, and results indicate the presence of $\text{K}_8\text{Cl}_2\text{Br}_6$ significantly reduce the energy barrier in the removal of metal species in MOF (a, c, e, g *vs.* b, d, f, h). According to the results, the removal of Zn from MOF to form $\text{CuN}_4/\text{vacN}_4@\text{NC-K}_{16}\text{Cl}_4\text{Br}_{12}$ is most favourable because of its lower energy barrier (-0.54 vs 0.12 eV). Specifically, the remarkable decomposition energy differences (Supplementary Fig. 19) between Zn atom (-0.54 eV) and ZnN_4 (20.99 eV) suggest the Zn species are removed dominantly in atomic state.

Electronic property of $\text{CuN}_4/\text{CoN}_4@\text{NC}$

Considering the possible configurations of CuN_4 and CoN_4 sites in $\text{CuN}_4/\text{CoN}_4@\text{NC}$, three potential model structures ($\text{CuN}_4/\text{CoN}_4@\text{NC}$, $\text{CuN}_4/\text{CoN}_4@\text{NC}(2N)$, $\text{CuN}_4/\text{CoN}_4@\text{NC}(ON)$) were established (Supplementary Fig. 20). The molecular dynamics simulations were conducted at 450 K for 20 ps upon these models to evaluate the thermodynamic stability (Supplementary Fig. 21). The fluctuation of total energy is clearly observed oscillating around the equilibrium state without structural disruption, verifying the reliable thermodynamic stability of these models. Considering the homogeneous distribution throughout the composite, the $\text{CuN}_4/\text{CoN}_4@\text{NC}$ model (Supplementary Fig. 20c) is selected for subsequent investigations. The charge distributions of $\text{CuN}_4@\text{NC}$, $\text{CoN}_4@\text{NC}$, and $\text{CuN}_4/\text{CoN}_4@\text{NC}$ are simulated (Supplementary Fig. 22) along with the corresponding Bader charges calculated (Supplementary Table 8). These results imply the synergistic interactions between CuN_4 and CoN_4 in $\text{CuN}_4/\text{CoN}_4@\text{NC}$ lead to remarkable electron accumulations and shifting in the density of states (DOS, Supplementary Fig. 23) of Co and Cu.

Catalytic performances in the synthesis of flavone

Flavone (also known as 2-phenylchromone) and derivatives are a class of natural compounds possessing fantastic biological activities like anticancer, antitumor, antibacterial, antimicrobial, antioxidant, estrogenic, and antiestrogenic properties, therefore are widely utilized in drug-relevant and biomedical fields^{21–24}. Accordingly, tremendous efforts have been devoted to synthesizing such β -*O*-substituted unsaturated ketones. Homogeneous routes like Baker-Venkataraman rearrangement, Kostanecki-Robinson reaction, Allan-Robinson, and Claisen condensation attained significant advances while suffering from harsh reaction conditions and the use of corrosive additives (e.g., strong acids or bases) or toxic oxidants (e.g., iodine-containing compounds, chromate, permanganate, pyochloride, and 2,3-dichloro-

5,6-dicyano-1,4-benzoquinone (DDQ)). In heterogeneous systems, palladium-based catalysts are demonstrated effective, but it is difficult to directly synthesize flavones with various substituted functional groups (to adjust the corresponding medicinal effects). In view of synthetic versatility, atom economy and environmental benign, it is highly desired to develop heterogeneous catalytic systems for highly efficient preparation of flavones.

Here, a domino catalytic system is developed for the general synthesis of flavones, as exemplified by the conversion of benzaldehyde and 2'-hydroxyacetophenone into flavone (Supplementary Figs. 24–26) over $\text{CuN}_4/\text{CoN}_4@\text{NC}$. The domino transformation consists of aldol condensation, intramolecular cyclization and oxidative dehydrogenation (ODH) with 2'-hydroxychalcone and flavanone as the intermediates (Fig. 4a, d). The benzaldehyde conversion, flavone selectivity and yield are calculated according to Eqs. (1–3). Typically, the reaction was carried out at 140 °C under 2 bar O_2 . No flavone product is detected in the blank run without catalyst (Supplementary Table 9, entry 1). The negligible flavone yield over NC obtained via the pyrolysis of ZIF-8 (Supplementary Fig. 27) excludes the contribution of possible Zn residue (Supplementary Table 9, entry 2). To our delight, $\text{CuN}_4/\text{CoN}_4@\text{NC}$ is highly active and selective in this reaction, giving a complete benzaldehyde conversion and 99% flavone yield (Supplementary Table 9, entry 3). In contrast, Cu- and Co-based counterparts including $\text{CuN}_4@\text{NC}$, $\text{CoN}_4@\text{NC}$, $\text{Co}_x@\text{NC}$, $\text{Cu}_x/\text{Co}_x@\text{NC-750}$, Cu-ZIF-8-750 , Co-Ph-750 , Co-ZIF-8-750 , 600-Cu/Co@NC and 900-Cu/Co@NC , (Supplementary Figs. 4, 5, 14, 28–33, and Supplementary Tables 1, 2) all show unsatisfied catalytic performances (Supplementary Table 9, entries 4–12). In particular, only 55% benzaldehyde conversion and 32% flavone yield are obtained over $\text{Cu}_x/\text{Co}_x@\text{NC-750}$ (Supplementary Table 9, entry 7), indicating the key role of well-defined atomic sites in the catalytic reaction. Similar tendency is also observed for Cu-ZIF-8-750 or Co-Ph-750 , on which the flavone yields are much lower as compared with $\text{CuN}_4@\text{NC}$ or $\text{CoN}_4@\text{NC}$, respectively. The moderate activity of a physical mixture of $\text{CuN}_4@\text{NC}$ and $\text{CoN}_4@\text{NC}$ (Supplementary Table 9, entry 8) suggests the essential role of synergistic interactions between the adjacent CuN_4 and CoN_4 sites in pursuing high flavone yields. The unsatisfied catalytic performances of 600-Cu/Co@NC and 900-Cu/Co@NC indicate the critical impact of pyrolysis temperature. The reaction under N_2 atmosphere gives negligible flavone while significant amount of flavanone, implying the transformation of the flavanone intermediate requires aerobic condition (Supplementary Table 9, entry 13). As expected, the reaction using flavanone as the substrate proceeds smoothly and affords similar flavone yield over $\text{CuN}_4/\text{CoN}_4@\text{NC}$ (Fig. 4b and Supplementary Table 10).

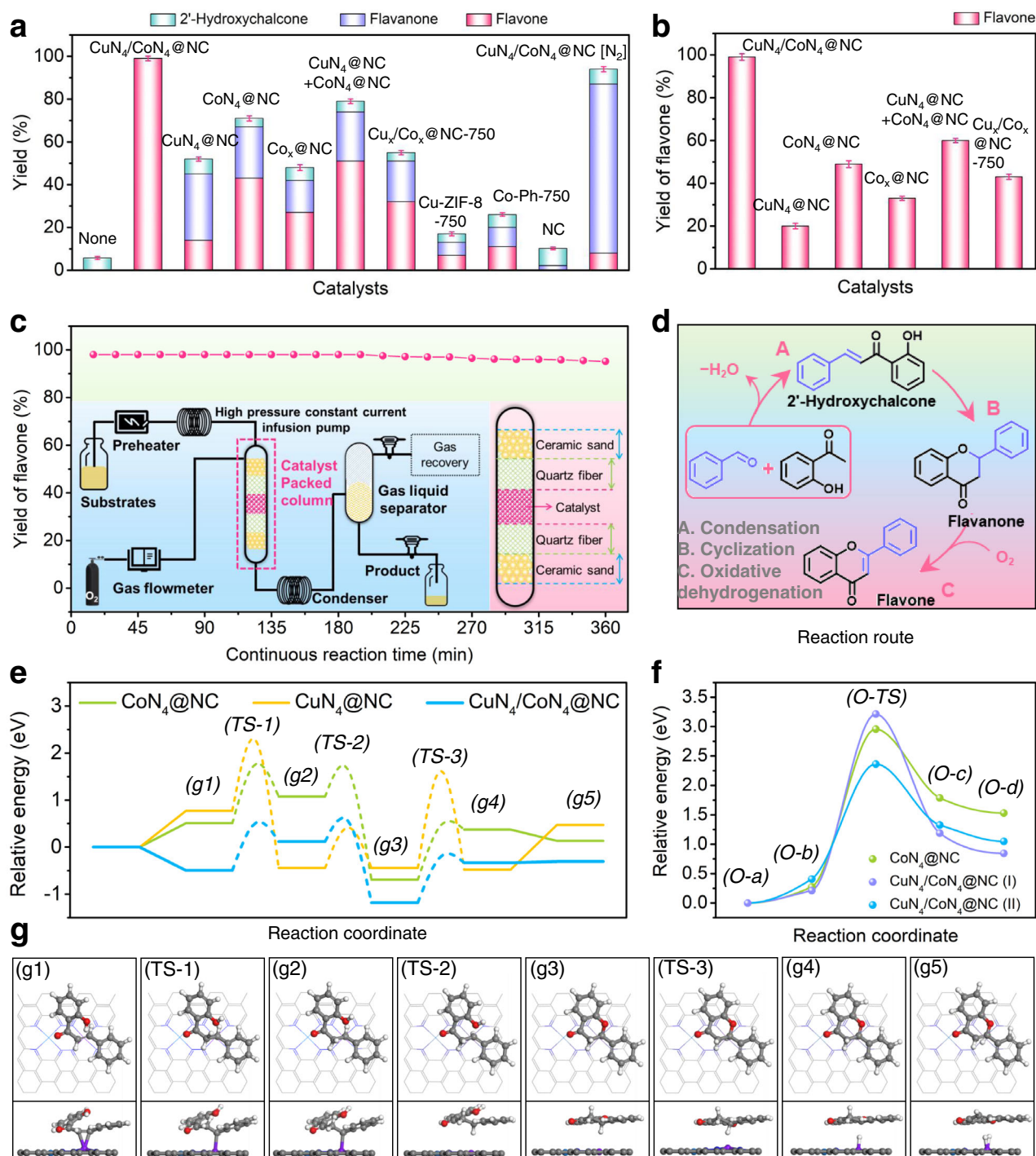


Fig. 4 | Catalytic performance of CuN₄/CoN₄@NC and reaction mechanistic studies. **a** Domino reaction of benzaldehyde and 2'-hydroxyacetophenone to flavone over different catalysts. **b** Oxidative dehydrogenation of flavanone to flavone over different catalysts. **c** Reaction results obtained in the continuous flow reactor (inset: simplified diagram of the reactor (left) and detailed description of catalyst packed column (right)). **d** Proposed reaction routes. **e** Free energy diagram and

g atomistic structures of the initial state, transition state, and final state for the reaction pathways from 2'-hydroxychalcone to flavone on CuN₄/CoN₄@NC. The grey, blue, sky blue, purple, red, and white balls represent C, N, Cu, Co, O, and H atoms, respectively. "TS" denotes a transition state. **f** CI-NEB results of O₂ dissociation. The error bars represent standard deviation based on three measurements.

Continuous flow synthesis

To demonstrate the applicability of the catalytic system, CuN₄/CoN₄@NC was loaded into a continuous flow reactor (Fig. 4c). To our delight, nearly quantitative flavone yield is obtained within 360 min of reaction without any by-product detected, achieving a turnover number (TON) as high as 3842 (Eq. 4) and a space time yield (STY) of 66.7 g·g_{cat}⁻¹·h⁻¹ (Eq. 5). To the best of our knowledge, this work

represents an example of heterogeneous domino catalysis synthesis of flavones in a continuous flow reactor, showing great potential for practical application.

Reusability of CuN₄/CoN₄@NC

After reaction, CuN₄/CoN₄@NC was easily collected by centrifugation and directly reused for next runs. No obvious activity loss is observed

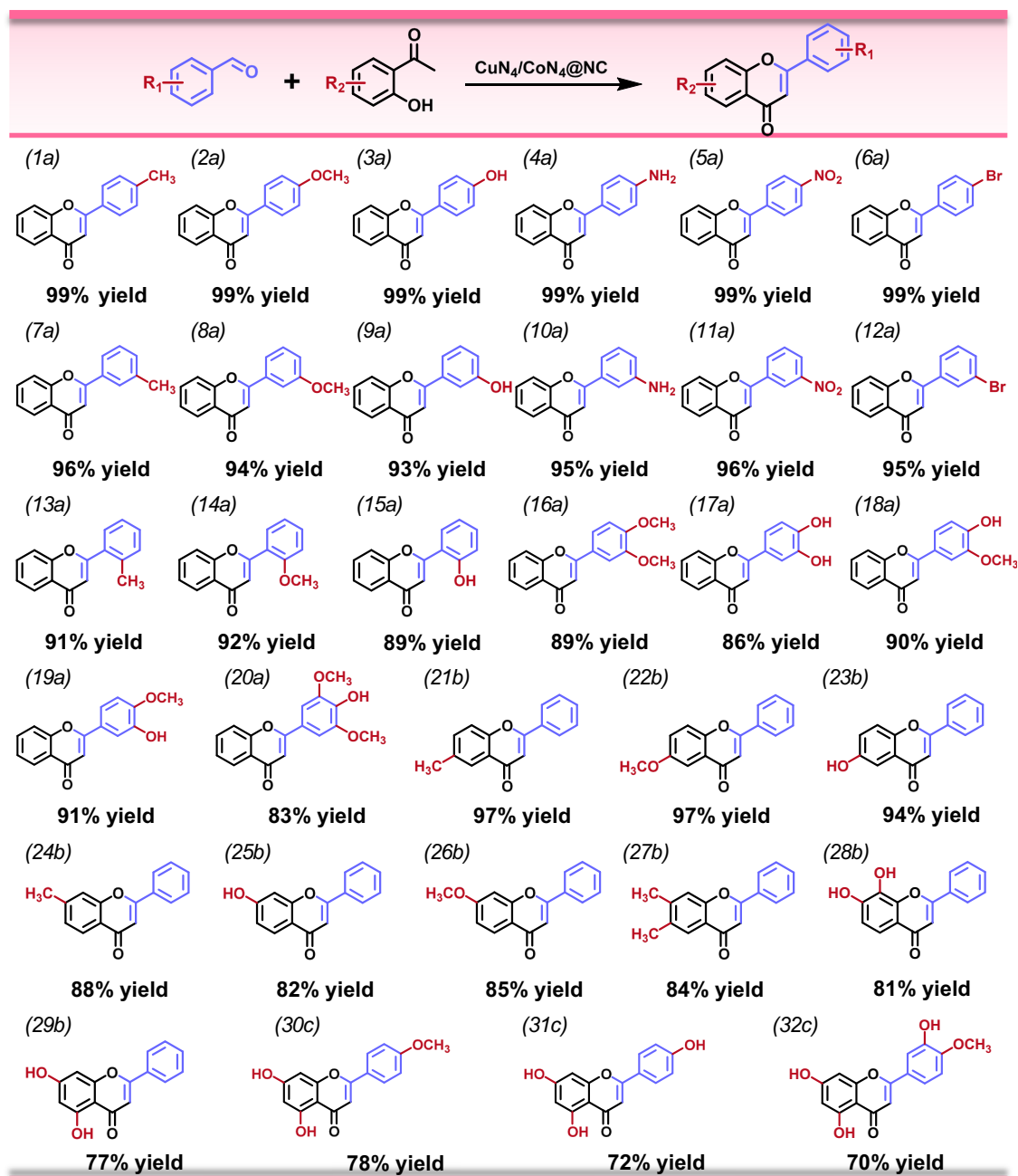


Fig. 5 | Scope of the domino reaction to various flavones. Reaction conditions: aldehyde (1 mmol), ketone (1.5 mmol), catalyst (total metal, 1.4 mol%), *n*-hexanol (4 mL), O₂ (2 bar), 140 °C, 12 h. Conversion and yield were determined by GC-MS based on aldehydes.

after reused for at least six times (Supplementary Fig. 34a), indicating its good recyclability. Characterization results including AC HAADF-STEM and XANES (Supplementary Figs. 35, 36, Supplementary Table 11) confirm the unchanged structural and compositional properties of the used CuN₄/CoN₄@NC in comparison with the fresh one. In addition, the metal leaching examination (Supplementary Table 2) and hot filtration experiment (Supplementary Fig. 34b) results also demonstrate the reliable durability of CuN₄/CoN₄@NC and the heterogeneous nature of the developed domino reaction system. These results indicate the obtained hetero-SAs are stable under the investigated reaction conditions.

Reaction mechanism

DFT calculations were conducted to gain theoretical insights into the reaction mechanism of the domino synthesis of flavone over

CuN₄/CoN₄@NC. Considering the aldol condensation of benzaldehyde and 2'-hydroxyacetophenone to 2'-hydroxychalcone is a common and simple reaction, the mechanism investigation begins with 2'-hydroxychalcone transformation. The entire reaction process consists of eight elementary steps (Fig. 4e, g, and Supplementary Figs. 37–39). At first, one 2'-hydroxychalcone molecule is adsorbed onto the CoN₄ site of CuN₄/CoN₄@NC (CoN₄ for CoN₄@NC and CuN₄ for CuN₄@NC) via the C=C group to form (g1). The adsorption energy over CuN₄/CoN₄@NC is negative (−0.50 eV), significantly lower than that of CuN₄@NC (0.77 eV) and CoN₄@NC (0.51 eV). The adsorbed 2'-hydroxychalcone molecule undergoes an intramolecular reaction through (TS-1) to form (g2), overcoming a relatively low energy barrier of 1.01 eV (1.25 eV for CoN₄@NC and 1.51 eV for CuN₄@NC). Afterwards, (g2) is easily transformed into (g3) (flavone) via an intramolecular cyclization process through (TS-2), the energy barrier is as low

as 0.43 eV (0.57 and 0.86 eV for $\text{CoN}_4@NC$ and $\text{CuN}_4@NC$, respectively). Subsequently, (g3) is dehydrogenated into (g4) through (TS-3). This step is also facilitated over $\text{CuN}_4/\text{CoN}_4@NC$ in comparison with $\text{CoN}_4@NC$ and $\text{CuN}_4@NC$ due to the reduced energy barrier (0.99 vs 1.16 and 2.06 eV). Finally, the generation of (g5) (*flavone) undergoes a dehydrogenation process, which is endothermic over $\text{CuN}_4/\text{CoN}_4@NC$ (0.13 eV) and $\text{CuN}_4@NC$ (0.47 eV) while exothermic over $\text{CoN}_4@NC$ (-0.31 eV).

Moreover, the O_2 activation mechanism was also investigated (Supplementary Table 11). Projected density-of-states (PDOS) are calculated to elucidate interactions between O_2 molecular orbitals and d orbitals of the metal center in the catalysts (Supplementary Fig. 40). When O_2 is adsorbed on CuN_4 , the O and Cu atom orbitals contribute to PDOS separately, indicating the physical adsorption of O_2 . DFT results reveal an O_2 adsorption energy of -0.22 eV over $\text{CuN}_4@NC$ with a 0.125 nm O-O bond length. On the other hand, after O_2 adsorption upon CoN_4 , characteristic peaks of O atom orbitals (-7.5 to -5 eV for π bond and -2 to 2 eV for π^* bond) become broad and weak. Besides, the π^* bond of O atom orbitals contributed by p_z and p_x orbitals of O atoms are overlapped by d_{z^2} and d_{xz} orbital of Co center, respectively, and all these orbitals contribute to the PDOS. These results suggest the formation of Co-O bonds, in other words, O_2 is chemically adsorbed on CoN_4 . The chemical adsorption of O_2 over $\text{CoN}_4@NC$ and $\text{CuN}_4/\text{CoN}_4@NC$ leads to reduced adsorption energy (-0.88 eV and -0.82 eV, respectively) and increased O-O bond length (0.129 nm). Moreover, O_2 adsorption causes remarkable charge redistribution in O_2 molecule and Co sites, and the O-O bond is weakened with the Co-O bonds newly formed (Supplementary Fig. 41). After O_2 adsorption, the electron depletion around CoN_4 is enhanced in $\text{CuN}_4/\text{CoN}_4@NC$ relative to $\text{CoN}_4@NC$, which is concerned beneficial for the subsequent O_2 disassociation.

Climbing Image Nudged Elastic Band (CI-NEB) method was utilized to explore the transition state and activation energy during O_2 disassociation (Fig. 4f, Supplementary Fig. 42 and Supplementary Table 12). For $\text{CoN}_4@NC$, the adsorbed O_2 is dissociated into two O atoms overcoming the activation energy barrier of 2.96 eV. One of the resultant O atoms locates at the top of CoN_4 and the other moves to the bridge site of the closest C-C bond, and the dissociation energy was 1.53 eV. In terms of $\text{CuN}_4/\text{CoN}_4@NC$, two potential configurations (I and II) are proposed requiring different activation energy barriers (3.21 eV and 2.36 eV, respectively), i.e., one O atom is stabilized on CoN_4 and the other may be captured by the second closest C-C bond (configuration I) or the closest carbon (configuration II), with a dissociation energy of 0.85 eV and 1.05 eV, respectively. Hence, the O_2 dissociation is much easier to take place over $\text{CuN}_4/\text{CoN}_4@NC$ through configuration II due to its lower energy barrier. To identify the reactive oxygen species (ROS) generated during the reaction, electron paramagnetic resonance (EPR) experiments were conducted over the reaction solution fetched online with the addition of 5,5-dimethyl-1-pyrroline N-oxide (DMPO) (Supplementary Fig. 43). The remarkable sextet EPR signal of DMPO-OOH (a spin adduct derived from $\text{DMPO} \cdot \text{O}_2$) confirms the formation of $\cdot\text{O}_2^-$ radicals²⁵, indicating the disassociation of molecular O_2 features $\cdot\text{O}_2^-$ radicals as the intermediate.

Based on the above results and discussions, the domino reaction could be divided into two main steps, O_2 activation and 2'-hydroxyacetophenone transformation. The two steps are almost equally important to attain the overall catalytic efficiency. The as-synthesized $\text{CuN}_4/\text{CoN}_4@NC$ exhibits improved capability in reducing energy barriers for both steps as compared with the counterparts, thus achieving significantly enhanced catalytic performance in the entire domino reaction.

Substrate scope

Substrate adaptability is a critical parameter to evaluate the versatility and efficiency of a catalytic system. In this work, various aromatic aldehydes and ketones with one to three substituted functional groups

were employed as substrates to investigate the general applicability of $\text{CuN}_4/\text{CoN}_4@NC$. For the aldehydes with one substituted group (including electron-donating and electron-withdrawing ones), excellent yields (89–99%) of the corresponding flavones are obtained (Figs. 5, 1a–15a). With two substituted groups on the aromatic aldehydes, the products yields are 83–91% (Figs. 5, 16a–20a). On the other hand, the domino reactions between benzaldehyde and substituted 2'-hydroxyacetophenone also proceed smoothly (Figs. 5, 21b–29b), further demonstrating the substrate scope of flavones synthesis. Moreover, flavone derivatives with multiple substituents can also be obtained in moderate to good yields (70–78%) over $\text{CuN}_4/\text{CoN}_4@NC$ (Figs. 5, 30c–32c).

The wide substrate scope of $\text{CuN}_4/\text{CoN}_4@NC$ further demonstrates its high efficiency in synergistically catalyzing the domino reaction to produce substituted flavones with fantastic biological activities. For instance, chrysin (Figs. 5, 29b) features a wide range of pharmacological activities including anti-tumor, anti-allergic, antiviral, and hypoglycemic effects. It is also confirmed effective in inhibiting HIV activation in latent infection model. Acacetin (Figs. 5, 30c) is naturally synthesized in chamomile tea, which shows effective anti-cancer activity via inducing cancer cell cycle arrest, apoptosis and autophagy. Apigenin (Figs. 5, 31c) is a natural antioxidant existing in chamomile tea, which is effective in lowering blood pressure, relaxing blood vessels, and inhibiting tumors. Diosmetin (Figs. 5, 32c) is a natural flavonoid in lemon possessing anti-oxidant, and anti-mutation biological activities, which can suppress the activation of carcinogens by inhibiting CYP1A1 enzyme. Notably, $^1\text{H-NMR}$ and $^{13}\text{C-NMR}$ spectra (Supplementary Figs. 44–51) are employed to identify these products.

Discussion

In summary, a versatile medium-induced infiltration deposition strategy is developed for the fabrication of a variety of metal SAs or dual-metal hetero-SAs affixed on hierarchically porous N-doped carbons. The underlying mechanism of composition and structure evolution during the materials preparation uncovers the essential roles of molten salt medium as the carrier of precursor, pore generator and metal stabilizer. The high catalytic efficiencies of the as-obtained hetero-SA catalysts (especially $\text{CuN}_4/\text{CoN}_4@NC$) are demonstrated in the domino synthesis of flavone and 32 kinds of derivatives from substituted benzaldehydes and 2'-hydroxyacetophenones, achieving an STY of 66.7 g \cdot g $_{\text{cat}}^{-1}\cdot$ h $^{-1}$ for flavone in a flow reactor. Reaction mechanism studies suggest the attractive catalytic performance over $\text{CuN}_4/\text{CoN}_4@NC$ is ascribed to the promoted O_2 activation-dissociation capability and reduced energy barriers of critical elementary steps in the synthesis of flavones. This work might provide insights into the highly efficient synthesis of natural products like flavones as demonstrated here.

Methods

Chemicals

All chemicals were purchased from commercial sources and directly used without further purification. Zinc acetate dihydrate ($\text{Zn}(\text{OAc})_2 \cdot 2\text{H}_2\text{O}$, 99.99%, Aladdin), copper acetate monohydrate ($\text{Cu}(\text{OAc})_2 \cdot \text{H}_2\text{O}$, 99%, Aladdin), cobalt acetate tetrahydrate ($\text{Co}(\text{OAc})_2 \cdot 4\text{H}_2\text{O}$, 99.99%, Aladdin), nickel acetate tetrahydrate ($\text{Ni}(\text{OAc})_2 \cdot 4\text{H}_2\text{O}$, 99%, Aladdin), manganese acetate tetrahydrate ($\text{Mn}(\text{OAc})_2 \cdot 4\text{H}_2\text{O}$), 2-methylimidazole (2-MI, 98%, Aladdin), potassium bromide (KBr, 99.5%, Aladdin), potassium chloride (KCl, 99.5%, Aladdin), cobalt phthalocyanine (Co-Ph, 95%, Aladdin), copper phthalocyanine (Cu-Ph, 90%, Aladdin), and iron phthalocyanine (Fe-Ph, 97%, Aladdin).

Synthesis of ZIF-8, Co-ZIF-8, Cu-ZIF-8, Ni-ZIF-8, and Mn-ZIF-8

In a typical synthesis, 2-methylimidazole (2-MI, 0.068 mol) was dissolved in 25 mL deionized water and stirred for 5 min at room temperature. Afterwards, a 25 mL aqueous solution containing $\text{Zn}(\text{OAc})_2 \cdot 2\text{H}_2\text{O}$ (0.0068 mol) was added to the above solution.

After a 5-h aging process, the white powder was collected through centrifugation and washing with methanol for three times to obtain ZIF-8.

Cu-ZIF-8, Co-ZIF-8, Ni-ZIF-8, and Mn-ZIF-8 were synthesized by the same recipe with the addition of 0.15 g of corresponding metal source (Co(OAc)₂·4H₂O, Cu(OAc)₂·4H₂O, Ni(OAc)₂·4H₂O, Mn(OAc)₂·4H₂O).

Synthesis of CuN₄/CoN₄@NC, M_aN₄/M_bN₄@NC, 600-Cu/Co@NC and 900-Cu/Co@NC

Typically, the as-prepared Cu-ZIF-8 was mixed with 0.02 g Co-Ph and 60 equivalent weights of KCl-KBr salt (KCl: KBr = 1: 3 by weight). The mixture was placed in a tubular furnace and heated to 750 °C at a ramp rate of 2 °C min⁻¹ and kept for 60 min under Ar atmosphere. CuN₄/CoN₄@NC was obtained after thoroughly washing by deionized water.

The M_aN₄/M_bN₄@NC composites were synthesized by the same recipe except for using different ZIFs and/or metal-Ph sources (e.g., Co-ZIF-8, Cu-ZIF-8, Ni-ZIF-8, Mn-ZIF-8, Cu-Ph, Co-Ph, and Fe-Ph).

The 600-Cu/Co@NC and 900-Cu/Co@NC were synthesized by the same recipe except for heated to 600 °C and 900 °C, respectively.

Synthesis of CuN₄@NC

Typically, the as-prepared Cu-ZIF-8 was mixed with 60 equivalent weights of KCl-KBr salt (KCl: KBr = 1: 3 by weight). The mixture was heated to 750 °C at a ramp rate of 2 °C min⁻¹ and kept for 60 min under Ar atmosphere in a tubular furnace. CuN₄@NC was obtained after thoroughly washing by deionized water.

Synthesis of CoN₄@NC

Typically, the as-prepared ZIF-8 was mixed with 0.02 g Co-Ph and 60 equivalent weights of KCl-KBr salt (KCl: KBr = 1: 3 by weight). The mixture was heated to 750 °C at a ramp rate of 2 °C min⁻¹ and kept for 60 min under Ar atmosphere in a tubular furnace. CoN₄@NC was obtained after thoroughly washing by deionized water.

Synthesis of Co_x@NC

Typically, 0.02 g Co-Ph was mixed with KCl-KBr salt (KCl: KBr = 1: 3 by weight). The mixture was placed in a tubular furnace and heated to 750 °C at a ramp rate of 2 °C min⁻¹ and kept for 60 min under Ar atmosphere. Co_x@NC was obtained after thoroughly washing with deionized water.

Synthesis of NC

Typically, the as-prepared ZIF-8 was mixed with 60 equivalent weights of KCl-KBr salt (KCl: KBr = 1: 3 by weight). The mixture was loaded to a tubular furnace and heated to 750 °C at a ramp rate of 2 °C min⁻¹ and kept for 60 min under Ar atmosphere. NC was obtained after thoroughly washing by deionized water.

Synthesis of Cu_x/Co_x@NC-750

Typically, a mixture of Cu-ZIF-8 (0.13 g) and Co-Ph (0.02 g) was placed in a tubular furnace and heated to 750 °C using a ramp rate of 2 °C min⁻¹ and kept for 60 min under Ar atmosphere to obtain Cu_x/Co_x@NC-750.

Synthesis of Cu-ZIF-8-750 and Co-Ph-750

Typically, Cu-ZIF-8 was placed in a tubular furnace and heated to 750 °C at a ramp rate of 2 °C min⁻¹ and kept for 60 min under Ar atmosphere to obtain Cu-ZIF-8-750.

The Co-Ph-750 was prepared according to the same recipe except for using Co-Ph as the precursor.

Materials characterization

The size and morphology of materials were studied by scanning electron microscopy (SEM) and transmission electron microscopy

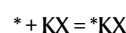
(TEM). SEM was carried out on a HITACHI SU8220 instrument. TEM and high-angle annular dark-field scanning transmission electron microscopy (HAADF-STEM) were recorded on a FEI Titan Cubed Themis G² 300 S/TEM with a probe corrector and a monochromator at 200 kV. Powder X-ray diffraction (XRD) patterns of the samples were obtained on a Rigaku diffractometer (D/max-III A, 3 kW) with CuKα radiation (λ = 1.5406 Å) at a voltage of 40 kV and a current of 10 mA at room temperature. Raman spectra were recorded on a LabRAM ARAMIS Raman spectrometer (HORIBA Jobin Yvon). Brunauer Emmett Teller (BET) surface area and pore size measurements were performed on a Micromeritics ASAP 2020 M instrument at 77 K. Before the analysis, the samples were degassed at 50 °C for 12 h. X-ray photoelectron spectroscopy (XPS) was collected on a Thermo Scientific K-Alpha system with the C 1s peak (284.6 eV) as reference. The metal contents of the samples were determined by ICP-OES on an Optima 8300 instrument. Thermogravimetric analysis (TG) was performed on a NETZSCH STA449C instrument loaded with 5 mg sample using a heating rate of 5 °C/min under argon atmosphere. The C and N elemental contents of the samples were measured on a Euro Vector EA3000 instrument (EA). The X-ray absorption experiments were carried out at the XAS station (BL14W1) of the Shanghai Synchrotron Radiation Facility (SSRF). The electron storage ring was operated at 3.5 GeV. Si (311) double-crystal was used as the monochromator, and the data was collected using solid-state detector under ambient conditions. The beam size was limited by the horizontal and vertical slits with the area of 1 × 4 mm² during XAS measurements.

Calculation details

Molecular dynamics (MD) simulations were carried out with Forcite Plus of Materials Studio software (Biovia Inc.). The temperature was controlled at 450 K by a Nose thermostat. The dynamics of 10 ps was carried out with NVT ensemble, and the time step was set as 1 fs. Van der Waals interactions were calculated by an atom-based method with a cutoff distance of 12.5 Å. Electrostatic interactions were calculated by the Ewald method, which takes a long time but is accurate for long-range interactions. Finally, the change of the model structure in the kinetic process is analyzed to judge the thermodynamic stability of the model at 450 K.

Spin-polarized density functional theory (DFT) calculations were performed with the Vienna ab initio simulation package (VASP), using projector augmented wave (PAW) pseudopotential for the core electrons, a cutoff energy (450 eV) for the valence electrons, and the generalized gradient approximation (GGA) in the form of Perdew-Burke-Ernzerhof (PBE) for the exchange correlation potentials. All models were constructed based on a rectangle graphene supercell with lattice constants *a* and *b* as 12.78 and 12.30 Å, containing 60 carbon atoms. To avoid interactions between adjacent images the *c* axis of these models is set to be 20 Å. The atoms were relaxed fully until the energy convergence reaches 0.00001 eV and the force acting on each atom was <0.01 eV/Å. The lattice constants of all models are relaxed, as well. Van der Waals interaction was considered at the DFT-D2 level as proposed by Grimme.

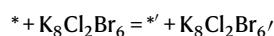
Coordinating tendency of metal ions to halogen anions was compared via the adsorption energy of KX ion pairs (X = Cl, Br), which is calculated according to the reaction,



$$E_{\text{ads}} = E_{*KX} - E_* - E_{KX}$$

where E_{*}, E_{KX}, and E_(*KX) are total energy of catalyst, KX ion pair, and catalyst with KX adsorbed. The leaving of metal ions (Cu, Zn) from

the catalyst to molten salts were characterized by energy change of the following reaction,



$$\Delta E = E_{-}(*') + E_{-}(\text{K}_8\text{Cl}_2\text{Br}_6') - E_{-}* - E_{-}\text{K}_8\text{Cl}_2\text{Br}_6$$

where * and $\text{K}_8\text{Cl}_2\text{Br}_6$ represent catalyst with metal ions and pure molten salts, while *' and $\text{K}_8\text{Cl}_2\text{Br}_6'$ represent catalyst without a metal ion and molten salts with a metal ion. The insertion of metal ion to the catalyst is defined as the reverse reaction of the above reaction.

Catalytic reaction of benzaldehyde and 2'-hydroxyacetophenone

In a typical run, benzaldehyde (1 mmol), 2'-hydroxyacetophenone (1.5 mmol), catalyst (1.4 mol% total metal relative to benzaldehyde), and *n*-hexanol (4 mL) were sealed in a high-pressure reactor (NSG25-P5-T3-SS1-SV, Anhui Kemi Machinery Technology Co., Ltd). The reactor was evacuated, refilled with 2 bar O_2 , and heated to 140 °C for 12 h under magnetic stirring. After reaction, the reactor was cooled to room temperature. The catalyst was isolated by centrifugation and directly reused after washing and drying. The product was quantified by a GC-MS spectrometer (Agilent, 7890B GC/5977 A MS) equipped with a DB-35 MS UI capillary column (0.25 mm × 30 m).

The conversion and selectivity are calculated using the following equations:

$$\text{Benzaldehyde conversion} = \left(1 - \frac{\text{Moles of benzaldehyde}}{\text{Moles of benzaldehyde loaded}}\right) \times 100\% \quad (1)$$

$$\text{Flavone selectivity} = \left(\frac{\text{Moles of flavone}}{\text{Moles of benzaldehyde converted}}\right) \times 100\% \quad (2)$$

$$\text{Flavone yield} = \left(\frac{\text{Moles of flavone}}{\text{Moles of benzaldehyde loaded}}\right) \times 100\% \quad (3)$$

Continuous flow synthesis of flavone

The continuous flow reactor is illustrated in the maintext (Fig. 4c). Before reaction, the $\text{CuN}_4/\text{CoN}_4@\text{NC}$ powder is pelletized, crushed, and sieved into particles in sizes of 20–30 mesh. And the flowing phase is formulated with reactant (benzaldehyde and 2'-hydroxyacetophenone in a molar ratio of 1:1.2) and *n*-hexanol solvent. In a typical run, the catalyst (100 mg) is loaded in the packed column and heated to 150 °C, followed by simultaneously feeding the flowing phase at 0.5 mL min⁻¹ and bubbling the O_2 at 30 mL (standard temperature and pressure, STP) min⁻¹ while maintaining the reaction pressure at 0.6 MPa.

The turnover number (TON) is calculated using the following equation:

$$\text{TON} = \frac{\text{Moles of benzaldehyde converted}}{\text{Moles of Co}} \quad (4)$$

The space time yield (STY) is calculated using the following equation:

$$\text{STY} = \frac{\text{Flavone mass}}{\text{Catalyst mass}} \times \frac{1}{\text{Reaction time}} \quad (5)$$

Data availability

The experimental data generated in this study are provided in the Supplementary Information file.

References

- Cui, X., Li, W., Ryabchuk, P., Junge, K. & Beller, M. Bridging homogeneous and heterogeneous catalysis by heterogeneous single-metal-site catalysts. *Nat. Catal.* **1**, 385–397 (2018).
- Li, Z. et al. Well-defined materials for heterogeneous catalysis: from nanoparticles to isolated single-atom sites. *Chem. Rev.* **120**, 623–682 (2020).
- Jin, R., Li, G., Sharma, S., Li, Y. & Du, X. Toward active-site tailoring in heterogeneous catalysis by atomically precise metal nanoclusters with crystallographic structures. *Chem. Rev.* **121**, 567–648 (2021).
- Zhao, Y. et al. Simultaneous oxidative and reductive reactions in one system by atomic design. *Nat. Catal.* **4**, 134–143 (2021).
- Han, L. et al. A single-atom library for guided monometallic and concentration-complex multimetallic designs. *Nat. Mater.* **21**, 681–688 (2022).
- Wang, X. et al. Atomically dispersed pentacoordinated-zirconium catalyst with axial oxygen ligand for oxygen reduction reaction. *Adv. Mater.* **34**, 2202240 (2022).
- Jiao, L. et al. Nanocasting SiO_2 into metal-organic frameworks imparts dual protection to high-loading Fe single-atom electrocatalysts. *Nat. Commun.* **11**, 2831 (2020).
- Jones, J. et al. Thermally stable single-atom platinum-on-ceria catalysts via atom trapping. *Science* **353**, 150–154 (2016).
- Li, Y. et al. Atomically dispersed dual-metal site catalysts for enhanced CO_2 reduction: mechanistic insight into active site structures. *Angew. Chem. Int. Ed.* **61**, e202205632 (2022).
- Shang, H. et al. Engineering unsymmetrically coordinated Cu- S_1N_3 single atom sites with enhanced oxygen reduction activity. *Nat. Commun.* **11**, 3049 (2020).
- Jin, H. et al. Unprecedentedly high activity and selectivity for hydrogenation of nitroarenes with single atomic $\text{Co}_1\text{-N}_3\text{P}_1$ sites. *Nat. Commun.* **13**, 723 (2022).
- Yuan, K. et al. Boosting oxygen reduction of single iron active sites via geometric and electronic engineering: nitrogen and phosphorus dual coordination. *J. Am. Chem. Soc.* **142**, 2404–2412 (2020).
- Rong, C. et al. Electronic structure engineering of single-atom Ru sites via Co- N_4 sites for bifunctional pH-universal water splitting. *Adv. Mater.* **34**, 2110103 (2022).
- Li, Y. et al. Loading single-Ni atoms on assembled hollow N-rich carbon plates for efficient CO_2 electroreduction. *Adv. Mater.* **34**, 2105204 (2022).
- Lu, X. F., Yu, L., Zhang, J. & Lou, X. W. Ultrafine dual-phased carbide nanocrystals confined in porous nitrogen-doped carbon dodecahedrons for efficient hydrogen evolution reaction. *Adv. Mater.* **31**, 1900699 (2019).
- Zhao, X., Fang, R., Wang, F., Kong, X.-P. & Li, Y. Metal oxide-stabilized hetero-single-atoms for oxidative cleavage of biomass-derived isoeugenol to vanillin. *ACS Catal.* **12**, 8503–8510 (2022).
- Wei, Y.-S. et al. Fabricating dual-atom iron catalysts for efficient oxygen evolution reaction: a heteroatom modulator approach. *Angew. Chem. Int. Ed.* **59**, 16013–16022 (2020).
- Cui, T. et al. Engineering dual single-atom sites on 2D ultrathin N-doped carbon nanosheets attaining ultra-low-temperature zinc-air battery. *Angew. Chem. Int. Ed.* **61**, e202115219 (2022).
- Ren, W. et al. Isolated diatomic Ni-Fe metal-nitrogen sites for synergistic electroreduction of CO_2 . *Angew. Chem. Int. Ed.* **58**, 6972–6976 (2019).

20. Yang, H. B. et al. Atomically dispersed Ni(I) as the active site for electrochemical CO₂ reduction. *Nat. Energy* **3**, 140–147 (2018).
21. Diao, T. & Stahl, S. S. Synthesis of cyclic enones via direct palladium-catalyzed aerobic dehydrogenation of ketones. *J. Am. Chem. Soc.* **133**, 14566–14569 (2011).
22. Zhu, F., Li, Y., Wang, Z. & Wu, X.-F. Iridium-catalyzed carbonylative synthesis of chromenones from simple phenols and internal alkynes at atmospheric pressure. *Angew. Chem. Int. Ed.* **55**, 14151–14154 (2016).
23. Zhao, D., Beiring, B. & Glorius, F. Ruthenium-NHC-catalyzed asymmetric hydrogenation of flavones and chromones: general access to enantiomerically enriched flavanones, flavanols, chromanones, and chromanols. *Angew. Chem. Int. Ed.* **52**, 8454–8458 (2013).
24. Yatabe, T., Jin, X., Yamaguchi, K. & Mizuno, N. Gold nanoparticles supported on a layered double hydroxide as efficient catalysts for the one-pot synthesis of flavones. *Angew. Chem. Int. Ed.* **54**, 1–6 (2015).
25. Wang, H. et al. Giant electron-hole interactions in confined layered structures for molecular oxygen activation. *J. Am. Chem. Soc.* **139**, 4737–4742 (2017).

Acknowledgements

This work was supported by the National Natural Science Foundation of China (21825802, 21908068, 22138003), the Natural Science Foundation of Guangdong Province (2017A030312005, 2020A1515010376), the Fundamental Research Funds for the Central Universities (2022ZY GXZR108), and the Introduced Innovative R&D Team Leadership of Dongguan City (2020607263005).

Author contributions

Y.L., R.F., and X.Z., conceived the idea and designed the experiments. R.F., X.Z., and Y.L. cowrote the manuscript. X.Z. and R.F. performed most of the experiments and characterizations. X.Z. and F.W. carried out the SEM and TEM characterizations. X.Z., R.F., and X.K. conducted the theoretical calculations. All the authors discussed the results and commented on the manuscript.

Competing interests

The authors declare no competing interests.

Additional information

Supplementary information The online version contains supplementary material available at <https://doi.org/10.1038/s41467-022-35598-3>.

Correspondence and requests for materials should be addressed to Ruiqi Fang or Yingwei Li.

Peer review information *Nature Communications* thanks Jie Xu and the other, anonymous, reviewers for their contribution to the peer review of this work.

Reprints and permissions information is available at <http://www.nature.com/reprints>

Publisher's note Springer Nature remains neutral with regard to jurisdictional claims in published maps and institutional affiliations.

Open Access This article is licensed under a Creative Commons Attribution 4.0 International License, which permits use, sharing, adaptation, distribution and reproduction in any medium or format, as long as you give appropriate credit to the original author(s) and the source, provide a link to the Creative Commons license, and indicate if changes were made. The images or other third party material in this article are included in the article's Creative Commons license, unless indicated otherwise in a credit line to the material. If material is not included in the article's Creative Commons license and your intended use is not permitted by statutory regulation or exceeds the permitted use, you will need to obtain permission directly from the copyright holder. To view a copy of this license, visit <http://creativecommons.org/licenses/by/4.0/>.

© The Author(s) 2022